1 **Revision 1**

2 **Phase relations of Fe-Mg spinels including new high-pressure post-spinel**

3 **phases and implications for natural samples**

4

5 LAURA UENVER-THIELE[1], ALAN B. WOODLAND[1], TIZIANA BOFFA BALLARAN[2],

6 NOBUYOSHI MIYAJIMA[2] AND DAN J. FROST[2]

7

8 [1] Institut für Geowissenschaften, Goethe-Universität Frankfurt, Altenhöferallee 1, D - 60438

9 Frankfurt am Main, Germany

10 [2] Bayerisches Geoinstitut, Universität Bayreuth, D - 95440 Bayreuth, Germany

11

14

15

16 **ABSTRACT**

17 Phase relations of magnesioferrite-magnetite solid solutions $(Mg,Fe^{2+})Fe^{3+}_2O_4$ were

18 investigated at pressures of 9–23 GPa and temperatures of 1200–1600 °C. Our new results

19 indicate that the assemblage $Mg_2Fe_2O_5 + Fe_2O_3$ reconstitutes to a hp-$MgFe_2O_4$ phase at 20

20 GPa and 1300–1500 °C. The stability field of hp-$MgFe_2O_4$ begins at ~1300 °C and widens to

21   higher temperature. At lower temperature (1200-1300 °C) $Mg_2Fe_2O_5 + Fe_2O_3$ breaks down to

22   the new phase assemblage $Mg_3Fe_4O_9 + Fe_2O_3$ with its stability field expanding to higher

23   pressures and temperatures at the expense of hp-$MgFe_2O_4$. The $Mg_3Fe_4O_9$ phase has the

24   same crystal structure that was recently reported for Fe_7O_9, and thus represents the Mg-

25   endmember. From powder X-ray diffraction, we find that hp-$MgFe_2O_4$ has a structure

26   consistent with an orthorhombic unit cell belonging to the *Pmcn* space group (No. 62).

27   However, it could have undergone a transformation from a different structure during

28   decompression.

29   Experiments conducted with a $Mg_{0.5}Fe^{2+}_{0.5}Fe^{3+}_2O_4$ composition demonstrate that the addition

30   of Fe^{2+} significantly changes the topology of the phase relations compared to the $MgFe_2O_4$

31   endmember system. At 10-11 GPa and 1000-1600 °C, $Mg_{0.5}Fe_{0.5}Fe_2O_4$ breaks down to the

32   assemblage $MgFeFe_2O_5 + Fe_2O_3$, with the phase boundary described by: P [GPa] = $2.0x10^{-3}$

33   x T [°C] + 8.2. No stability field for the constituent oxides [i.e. $(Mg,Fe)O + Fe_2O_3$] exists, in

34   contrast to that observed for the $MgFe_2O_4$ endmember. The stability of the assemblage

35    $MgFe^{2+}Fe^{3+}_2O_5 + Fe_2O_3$ is limited at higher pressures and appears to pinch out to higher

36   temperatures. At 15-16 GPa and temperatures up to 1350 °C, this assemblage reconstitutes to

37   form a hp-$Mg_{0.5}Fe_{0.5}Fe_2O_4$ phase. However, at higher temperatures a new assemblage of

38    $(Mg,Fe)_3Fe_4O_9 + Fe_2O_3$ appears. The occurrence of such compositions suggests that solid

39   solution may be complete across the $Mg_3Fe_4O_9$–Fe_7O_9 binary.

40   Our results further demonstrate that phase relations even in simple Fe-Mg oxides can become

41   complex at high pressures and temperatures and that phases with a variety of novel

42   stoichiometries (i.e. $Mg_3Fe_4O_9$) may become stable. In addition, this study has implications

43   for natural samples by helping to place constraints on the range in pressure and temperature at

44   which a given sample formed. For instance, magnetite or magnesioferrite entrapped as

45   inclusions in diamond could have either have crystallized directly, or formed from precursor

46 phases at depths that exceed the stability of the spinel-structured phases. Evidence for such

47 high-pressure transformations can potentially be found by investigating micro-textures.

48

49   **INTRODUCTION**

50 Spinel-structured oxides are of petrologic and geochemical interest because of their ability to

51 incorporate both trivalent and divalent cations such as Fe^{2+} and Fe^{3+}. Thus, their $Fe^{3+}/\Sigma Fe$

52 ratio can be used as an indicator of the prevailing oxygen fugacity (fO_2). Aside from

53 magnetite, incorporation of Mg, Al or Cr (e.g. $FeCr_2O_4$, $MgFe_2O_4$, $MgAl_2O_4$) makes such

54 oxides even more relevant to the Earth. A number of recent studies have demonstrated that

55 many spinel-structured phases have limited stability at conditions corresponding to depths >

56 ~300 km (Akaogi et al. 1999; Schollenbruch et al. 2011; Woodland et al. 2012; Ishii et al.

57 2014, 2015; Uenver-Thiele et al. 2017). An exception is ringwoodite [$(Mg,Fe)_2SiO_4$] that is

58 stable in the lower half of the transition zone between ~520 and 660 km depth (e.g. Frost,

59 2003). In a few cases, the breakdown products are the constituent oxides (i.e. $FeAl_2O_4$,

60 Schollenbruch et al. 2010, and $MgAl_2O_4$, Akaogi et al. 1999). In many other cases, so-called

61 "post-spinel" phases or assemblages become stable. For example, Chen et al. (2003) found

62 two different high-pressure (hp) polymorphs of $FeCr_2O_4$ in experiments at pressures above 12

63 and 20 GPa, respectively. Assemblages with phases having different stoichiometries have also

64 been reported, often involving a phase of $A_2B_2O_5$ stoichiometry coexisting with a B_2O_3

65 sequioxide (where A and B represent divalent and trivalent cations, respectively). Thus,

66 phases such as Fe_4O_5 (Lavina et al. 2011, Woodland et al. 2012) and $Mg_2Fe_2O_5$ (Boffa

67 Ballaran et al., 2015), as well as $Fe_2Cr_2O_5$ (Ishii et al. 2014, and $Mg_2Al_2O_5$ (Enomoto et al.

68 2009) also need to be considered as potential constituents of mantle assemblages. In addition,

69 the recently reported stability of new phases like Fe_5O_6 (Lavina & Meng 2015, Woodland et

70   al. 2015) and Fe_7O_9 (Sinmyo et al. 2016) further enlarge the variety of possible oxides that

71   could occur as accessory phases in the deep mantle.

72   Application of phase relations in chemically simple oxide systems can be found in

73   understanding the origin and evolution of inclusions in diamond. Such samples provide

74   important information not necessarily about the mantle as a whole, but at least about the

75   environment under which the diamond formed. For example, nearly pure magnetite has been

76   found as inclusions in diamonds from Mwadui, Tanzania (Stachel et al. 1998).

77   Magnesioferrite ($MgFe_2O_4$) has also been reported from a number of inclusions associated

78   with (Mg,Fe)O (McCammon et al. 1998, Harte et al. 1999, Wirth et al. 2014, Palot et al.

79   2016). These later occurrences are considered by the authors to have a lower mantle origin (or

80   at least transition zone). Based upon TEM observations, Wirth et al. (2014) suggested that the

81   magnesioferrite had transformed from a hp-$MgFe_2O_4$ phase during upwelling. However, the

82   phase relations of $MgFe_2O_4$ presented by Uenver-Thiele et al. (2017) exclude a direct phase

83   transition between a hp-phase and magnesioferrite. In fact no hp-$MgFe_2O_4$ was found to be

84   stable up to at least 18 GPa and 1000-1500 °C. Although Wirth et al. (2014) and Palot et al.

85   (2016) both refer to their phase as "magnesioferrite", the reported chemical analyses reveal

86   that they are in fact solid solutions. For the sample studied by Wirth et al. (2014), the

87   composition is very close to $Mg_{0.5}Fe_{0.5}Fe_2O_4$, therefore, interpretations based upon the

88   behavior of the $MgFe_2O_4$ endmember may be misleading. Predicting the effect of Fe^{2+} on

89   phase stabilities is complicated by the fact that post-spinel assemblages for the $FeFe_2O_4$

90   endmember are unquenchable, precluding detailed investigation (Woodland et al. 2012). The

91   aim of the present study was to investigate the phase relations of Fe_3O_4-$MgFe_2O_4$ solid

92   solutions up to ~23 GPa and temperatures relevant to the Earth's transition zone. This study

93   also included a set of experiments with $MgFe_2O_4$ bulk composition that extends the phase

94   relations described by Uenver-Thiele et al. (2017) to high pressures. Our new results allow us

95   to place more reliable constraints on the origin of "magnesioferrite" occurrences associated

96   with diamond formation.

97

EXPERIMENTAL METHODS

99   Starting materials for the high-pressure experiments were pre-synthesized $MgFe_2O_4$ and

100    $Mg_{0.5}Fe_{0.5}Fe_2O_4$. The magnesioferrite (unit-cell parameter a_o = 8.3875(1) Å) was the

101   same as that used in the study of Uenver-Thiele et al. (2017). A solid solution with a

102   composition of 50 mol% $MgFe_2O_4$ − 50 mol% $FeFe_2O_4$ was synthesized in a gas-mixing

103   furnace from a stoichiometric mixture of Fe_2O_3 and MgO. The oxide mixture was ground

104   together, pressed into pellets and equilibrated at 1100 °C and 1 bar in a 1:99 mixture of

105    $CO:CO_2$. This fixed the oxygen fugacity at $\log fO_2$= -8.5, which corresponds to the

106   condition where the magnetite component in the solid solution is stoichiometric

107   (Dieckmann, 1982). After 2 hrs, the sample was quenched in water and stored overnight at

108   120 °C. It was then reground, pressed into pellets and resintered for a further 5 hrs under

109   the same conditions. The black, fine-grained product was subsequently analysed by

110   electron microprobe and X-ray powder diffraction to verify homogeneity. A composition

111   of $Mg_{0.49(2)}Fe_{0.51(2)}Fe_2O_4$ with a unit-cell parameter of a_o = 8.3960(1) Å was obtained.

112   High-pressure and high-temperature experiments were carried out at the Universität Frankfurt

113   and the Bayerisches Geoinstitut, Bayreuth. A 800t Walker type multi-anvil press was

114   employed in Frankfurt. The experimental setup and pressure calibration is described by Brey

115   et al. (2008). For experiments performed at 18 GPa, the pressure was calibrated using the

116   wadsleyite to ringwoodite transformation in Mg_2SiO_4 (1200 °C, 18 GPa; Inoue et al. 2006).

117   Tungsten carbide anvils with truncated edge lengths of 4 mm or 8 mm were used along with

118   10 mm- or 14 mm-edged Cr_2O_3-doped MgO octahedra, respectively. At the Bayerisches

119   Geoinstitut, a 5000t multi-anvil press with tungsten carbide cubes with 8 or 11 mm truncation

120   length was used, together with 18mm-edged octahedra. In addition, several experiments were

121   conducted in a 1000t multi-anvil press. The pressure calibration for both presses, as well as

122   the detailed experimental setup is given in Keppler and Frost (2005). The assembly in

123   Frankfurt includes a Re-foil furnace, whilst a $LaCrO_3$ heater is employed in Bayreuth. A

124     $W_3/Re_{97}-W_{25}/Re_{75}$ thermocouple with the electromotive force uncorrected for pressure was

125   used to monitor the temperature. A heating rate of 50 °C/min was used. The experiments were

126   terminated by turning off the power and followed by decompression. Uncertainties in pressure

127   and temperature are ± 0.5 GPa and ± 30-50 °C, respectively (Keppler and Frost 2005). Fine-

128   grained starting materials were packed into Pt-foil capsules. Several experiments were

129   conducted with small amounts of PtO_2 (see Table 1) to ensure high oxygen fugacity during

130   the experimental run. The capsule design follows the description given in Uenver-Thiele et al.

131   (2017) to insure no incorporation of Pt into the sample.

132   Run products were analysed by electron microprobe (EPMA) and X-ray diffraction. Run

133   products as well as experimental run conditions are listed in Table 1. Microprobe analyses

134   were carried out with a five-spectrometer JEOL JXA-8900 Superprobe using pure MgO and

135   Fe_2O_3 as primary standards. The EPMA was operated in wavelength-dispersive mode with an

136   acceleration voltage of 15 kV, probe current of 20 nA and a spot size of 1 μm. Integration

137   time for Fe and Mg was 40 sec on the peak while an integration time of 20 sec and 40 sec on

138   the background was set for Fe and Mg, respectively. Where the grain size permitted, up to 4

139   analyses were performed on a single grain to verify homogeneity. A CITZAF algorithm was

140   employed for matrix correction (Armstrong 1993). Representative analyses are reported in

141   Table 2 (see supplementary data for the entire data set). Backscattered electron (BSE) images

142   were used to study the sample texture.

143   Powder X-ray diffraction patterns were obtained for some samples using a STOE Stadi P

144   diffractometer operating at 45 kV and 35 mA and using monochromatic Mo Kα (λ = 0.70926

145 Å) radiation, equipped with a linear PSD or a Mythen detector at the University of Frankfurt.

146 In this case, the samples were mounted in a 0.5 mm diameter capillary together with a small

147 amount of silicon that served as an internal standard. Diffraction patterns were collected in

148 transmission mode between 1°-100° 2 θ. For other samples, powder diffraction patterns were

149 measured with a Philips X´Pert PRO diffractometer employing monochromatic Co Kα (λ =

150 1.78897 Å) radiation selected with a focusing monochromator, a symmetrically cut curved

151 Johansson Ge (111) crystal and a Philips X'celerator detector at the Bayerisches Geoinstitut.

152 These samples were ground together with Si and dispersed on a Si wafer using ethanol. Data

153 were collected between 10° and 120° 2 θ at 40 kV and 40 mA. All patterns were analysed

154 with the General Structure Analysis System (GSAS, Larson and van Dreele 1994) software

155 package with the EXPGUI interface of Toby (2001) primarily for phase identification.

156 Transmission electron microscopic (TEM) investigations were carried out with a Philips

157 CM20FEG TEM, operated at 200 kV, at the Bayerisches Geoinstitut. Selected area electron

158 diffraction patterns of the hp-$MgFe_2O_4$ phase were obtained from powdered fragments taken

159 from the run product Z1234o and deposited on Lacey carbon coated copper grids.

160

RESULTS AND DISCUSSION

162

HIGH-PRESSURE PHASE RELATIONS OF $(Mg,Fe^{2+})Fe^{3+}_2O_4$

164

High-pressure behavior of $MgFe_2O_4$

166 The investigation of the phase relations in the system $MgFe_2O_4$ at pressures up to 23 GPa was

167 designed to complete the study presented by Uenver-Thiele et al. (2017) at pressures ≤ 18

168 GPa. The run conditions and results of the new high-pressure experiments are provided in

169 Table 1. Phase relations are presented in Figure 1.

170   The run products recovered from a series of experiments performed at 20 GPa (Table 1)

171   reveals different assemblages depending on temperature. At 1200 °C, very fine-grained MgO

172   + Fe_2O_3 (Fig. 2a) is the stable assemblage, consistent with the results of Uenver-Thiele et al.

173   (2017) at 18 GPa and the same temperature. At 20 GPa and 1400-1500 °C, the assemblage

174   $Mg_2Fe_2O_5$ + Fe_2O_3 was found. However, additional diffraction peaks have been observed in

175   the XRD pattern of this sample, indicating that a third phase is present. EPMA measurements

176   of this third phase give a composition of ~21 wt% MgO and ~73 wt% FeO that is consistent

177   with a $MgFe_2O_4$ stoichiometry (Tab. 2a). The coexistence of these three phases suggests that

178   we are likely close to the reaction boundary between $Mg_2Fe_2O_5$ + Fe_2O_3 and hp-$MgFe_2O_4$

179   (Fig. 1). This additional phase occurs as black tabular crystals up to 150 μm that are generally

180   strongly fractured (Fig. 2c). In the higher temperature experiment (H4349, Tab. 1) hp-

181   $MgFe_2O_4$ is much more abundant with only traces of $Mg_2Fe_2O_5$ + Fe_2O_3 observed in the

182   diffraction pattern.

183   In experiment Z1464o at 20 GPa and 1300 °C (Table 1), no $Mg_2Fe_2O_5$ was found in the run

184   products. The XRD pattern contains peaks corresponding to hematite and the hp-$MgFe_2O_4$

185   phase that was found at higher temperature. Here too, additional diffraction peaks are present

186   in the XRD pattern. Randomly oriented tabular crystals with cleavage exhibit a composition

187   consistent with hp-$MgFe_2O_4$ and appear to be the most abundant phase (Fig. 2b; Table 2a).

188   However, the texture of this sample indicates that the tabular grains have begun to break

189   down at the grain rims and within individual grains to a mixture of hematite and another

190   phase that is richer in Mg (darker grey phase in Fig. 2b). The phase composition of 27.1(8)

191   wt% MgO and 68.4(2) wt% FeO (Table 2a) corresponds to a $Mg_3Fe_4O_9$ stoichiometry. This

192   particular phase can also explain the additional peaks present in the diffraction pattern for this

193   sample that can be indexed using the monoclinic crystal structure recently reported for Fe_7O_9

194   by Sinmyo et al. (2016). The reason for this disequilibrium texture documenting the

195   breakdown of hp-$MgFe_2O_4$ lies with the loss of the thermocouple during the experiment and,

196   based upon previous experience, we suspect that the temperature decreased while operating

197   the LaCrO$_3$-heater at constant output power. As a consequence, the phase boundary between

198   hp-MgFe$_2$O$_4$ and Mg$_3$Fe$_4$O$_9$ + Fe$_2$O$_3$ could have been crossed (Fig. 1).

199   Powder XRD measurements and chemical analyses of the run products from the highest

200   pressure experiment (H4088, 23 GPa and 1500 °C) demonstrate that the sample is dominated

201   by the assemblage Mg$_3$Fe$_4$O$_9$ + Fe$_2$O$_3$, along with coexisting hp-MgFe$_2$O$_4$ (Fig. 3; Table 1).

202   BSE images reveal Mg$_3$Fe$_4$O$_9$ and hp-MgFe$_2$O$_4$ to be well crystallized as discrete grains with

203   hematite occurring as inclusions or on grain boundaries of Mg$_3$Fe$_4$O$_9$ (Fig. 2d-e). From these

204   results, it appears that the stability field of hp-MgFe$_2$O$_4$ phase is limited to ~23 GPa at 1500

205   °C by the equilibrium hp-MgFe$_2$O$_4$ = Mg$_3$Fe$_4$O$_9$ + Fe$_2$O$_3$. The stability field of hp-MgFe$_2$O$_4$

206   starts between 1200 and 1300 °C and expands towards higher temperature (see Fig. 1).

207   Although we can document the existence of the Mg-endmember of Fe$_7$O$_9$, a full assessment

208   of the stability field of the Mg$_3$Fe$_4$O$_9$ + Fe$_2$O$_3$ assemblage awaits further experiments at yet

209   higher pressures. However, we note that Sinmyo et al. (2016) produced Fe$_7$O$_9$ and

210   MgFe$^{2+}_2$Fe$^{3+}_4$O$_9$ at 24-26 GPa and 1600-1700 °C, suggesting that Mg$_3$Fe$_4$O$_9$ could be stable

211   at least up to these conditions as well.

212   Our results imply two further triple points in the MgFe$_2$O$_4$ system in addition to those

213   documented at < 18 GPa by Uenver-Thiele et al. (2017). Considering the experimental

214   uncertainties in temperature and pressure, the triple point where Mg$_2$Fe$_2$O$_5$, Fe$_2$O$_3$, hp-

215   MgFe$_2$O$_4$ and Mg$_3$Fe$_4$O$_9$ coexist should be at ~19-20 GPa and 1250-1300 °C. The other

216   triple point where MgO, Fe$_2$O$_3$, Mg$_2$Fe$_2$O$_5$ and Mg$_3$Fe$_4$O$_9$ coexist must lie at lower pressure

217   (~ 19 GPa) and at temperatures of 1200-1250 °C (Fig. 1). The stability of the assemblage

218   Mg$_3$Fe$_4$O$_9$ + Fe$_2$O$_3$ in the MgFe$_2$O$_4$ system highlights the fact that assemblages containing

219   phases of different stoichiometry have to be considered even in simple bulk compositions.

220

221   **Phase relations of 50 mol%MgFe$_2$O$_4$-50 mol%FeFe$_2$O$_4$ solid solution**

222 Sixteen multi anvil experiments using a starting composition of $Mg_{0.50(2)}Fe_{0.50(2)}Fe_2O_4$ were

223 performed between 9-20 GPa and 1000-1600 °C (Table 1). Textures of the run products and

224 the appearance of new assemblages confirmed that reaction occurred during each experiment

225 and equilibrium was reached (see Fig. 4a-f). In the three experiments conducted at pressures

226 below 11 GPa, a spinel solid solution was produced that had clearly recrystallized (Fig. 4a).

227 Its composition $(Mg_{0.49(1)}Fe_{0.51(1)}Fe_2O_4$, Table 2b) remained very similar to that of the

228 starting material, indicating that redox conditions were essentially constant during these

229 experiments. In the following discussion we refer to this spinel-structured phase as Mf50.

230 At pressures $\geq$ 11 GPa the spinel solid solution is no longer stable. BSE images of samples

231 M638 and M648 (Fig. 4b and 4c) indicate the presence of more than one phase. The

232 assemblage $(Mg,Fe)_2Fe_2O_5$ + hematite was confirmed by microprobe analysis and powder

233 XRD measurements. As illustrated in Figures 4b and 4c, $(Mg,Fe)_2Fe_2O_5$ changes from

234 having a lath-shape to more granular crystals going from 1100 °C to higher temperature (1500

235 °C). This change in habit must be related to some thermally activated change in grain growth

236 behavior rather than to a change in phase assemblage. The phase boundary defining the

237 breakdown of $Mg_{0.5}Fe_{0.5}Fe_2O_4$ to $MgFe^{2+}Fe^{3+}_2O_5$ + hematite has been bracketed to lie at 10-

238 11 GPa and between 1000-1600 °C (Fig. 5) and can be described with the following

239 expression:

240 $$P\,[GPa] = 2.0\text{x}10^{-3} \text{ x } T\,[°C] + 8.2$$

241   The position of this boundary is within uncertainties indistinguishable from that

242 documented for the Fe_3O_4 endmember breakdown reaction: $2\,Fe_3O_4 = Fe_4O_5 + Fe_2O_3$ (Fig.

243 4, Woodland et al. 2012, Schollenbruch et al. 2011). This stands in contrast to the Mg-

244 endmember system, where magnesioferrite is observed to first break down to other

245 assemblages before $Mg_2Fe_2O_5 + Fe_2O_3$ becomes stable (Fig. 5, Uenver-Thiele et al. 2017).

246 This boundary is not strictly univariant since, although the Mf50 phase stayed essentially on

247 composition, on the other side of the boundary $MgFe^{2+}Fe^{3+}_2O_5$ exhibits small shifts to higher

248 Fe^{2+} contents, resulting in solid solutions with $X_{Mg2Fe2O5}$ = 0.42-0.48 rather than the expected

249 0.5 (Table 2b). This change indicates that a small amount of reduction of Fe^{3+} to Fe^{2+}

250 occurred during the experiments since no buffering was possible for this mixed-valence bulk

251 composition, except the coexistence with Fe_2O_3 (Fig. 6a). However, this small shift in

252 composition should not appreciably affect the form of the phase relations depicted in Figure

253 5.

254 The stability field for ~$MgFe^{2+}Fe^{3+}_2O_5$ + hematite is limited at higher pressures and appears

255 to pinch out at high temperature. Experiment M648 is of particular interest as a phase

256 additional to $MgFe^{2+}Fe^{3+}_2O_5$ + hematite was identified first in the powder diffraction pattern

257 and subsequently by EPMA (Table 2b). Although it occurs as a minor constituent, diffraction

258 peaks could be indexed to the Fe_7O_9 structure reported by Sinmyo et al. (2016), similarly to

259 that described above for the $MgFe_2O_4$ system. Although it is possible that this new phase

260 formed as a consequence of reduction during the experiment, we note that such an additional

261 phase did not appear in any other experiment containing ~$MgFe^{2+}Fe^{3+}_2O_5$, where the run

262 products exhibit evidence for minor reduction. Therefore, we consider the conditions of this

263 experiment to lie on the phase boundary between the two assemblages $MgFe^{2+}Fe^{3+}_2O_5$ +

264 hematite and $(Mg,Fe)_3Fe_4O_9$ + hematite (Figs 5 and 6a). The stability of the assemblage

265 $(Mg,Fe)_3Fe_4O_9$ + Fe_2O_3 was confirmed in a further experiment at 15 GPa and ~1600 °C

266 (Z1584o), where large grains of both the O_9 phase and hematite have been recovered (Fig. 4e,

267 Table 1). Here, its composition of $Mg_{1.37(1)}Fe_{1.63(1)}Fe_4O_9$ deviates slightly from the expected

268 $Mg_{1.5}Fe_{1.5}Fe_4O_9$ stoichiometry, indicating that a small amount of reduction must have taken

269 place (Table 2b, Fig. 6b).

270 The hematite present in the different run products (Table 1) incorporates small amounts of Mg

271 (Tables 2a and 2b), as also reported by Uenver-Thiele et al. (2017) for experiments performed

272 with a $MgFe_2O_4$ bulk composition. Using a $Mg_{0.5}Fe_{0.5}Fe_2O_4$ starting composition, hematite

273 was found to contain up to 0.053 cations Mg per formula unit, corresponding to a maximum

274   mole fraction of $Mg_3O_3 = 0.018$ following the occupancy model of Berry et al. (1998, 2000).

275   This model involves the substitution of three Mg^{2+} cations for two Fe^{3+} cations, with the third

276   Mg^{2+} cation residing on a normally unoccupied site. Although the amount of Mg

277   incorporation increases slightly with temperature (Table 2b), its overall concentration is lower

278   than that observed by Uenver-Thiele et al. (2017). This is consistent with a lower activity of

279   MgO (a_{MgO}) expected for a bulk composition where half of the Mg has been replaced by Fe^{2+}.

280   Such limited Mg substitution in hematite should have only a negligible effect on the position

281   of the phase boundaries, lying within the uncertainties of the experimental conditions.

282   At lower temperatures of 1000-1400 °C a single phase, hp-$(Mg,Fe)Fe_2O_4$ becomes stable

283   (Fig. 5, Table 1). This phase is much more fine-grained compared to the Mf50 phase at low

284   pressures develops mostly a columnar habit (compare sample Z1585o with M654 illustrated

285   in Figs 4a and 4d). Different grain morphologies of hp-$(Mg,Fe)Fe_2O_4$ are observed above and

286   below 1300 °C, in a similar fashion to those described above for $(Mg,Fe)_2Fe_2O_5$ (compare

287   Fig. 4d and 4f). In several cases, small shifts in composition towards higher Fe^{2+} contents

288   reflect a minor amount of reduction in these experiments, and in Z1585o it led to the

289   production of traces of $(Mg,Fe)_3Fe_4O_9$ coexisting with a hp-$Mg_{0.47(2)}Fe_{0.53(2)}Fe_2O_4$ solid

290   solution (Table 2b, Fig. 6a and 6b).

291   In contrast to other high-pressure studies on $FeCr_2O_4$ and $MgAl_2O_4$ endmember

292   compositions (e.g. Ishii et al. 2014, Enomoto et al. 2008, Kojitani et al. 2010, Akaogi et al.

293   1999), we detected only one hp-polymorph with O_4-type stoichiometry between ~16-20 GPa

294   and 1000 −1600 °C. However, it is conceivable that additional high-pressure modifications

295   become stable at still higher pressure or temperature. The phase diagram illustrated in Figure

296   5 exhibits similarities and differences compared with the two endmember compositions

297    $FeFe_2O_4$ and $MgFe_2O_4$. For example, the breakdown of magnetite and the Mf50 phase takes

298   place at virtually the same pressure-temperature conditions, producing an assemblage of an

299   O_5-phase + hematite, whereas, magnesioferrite breaks down at only slightly lower pressure, it

300   does not react directly to an assemblage containing an O_5-type phase (Fig. 1). The assemblage

301   comprising the constituent oxides (i.e. $MgO + Fe_2O_3$) becomes destabilized by the addition of

302   Fe^{2+}, causing a significant change in the topology of the phase relations. The amount of Fe^{2+}

303   necessary for destabilizing this assemblage remains to be determined, but it is likely to be

304   rather small. A high-pressure phase with O_4-stoichiometry is confirmed to be stable for both

305   endmember compositions (Fei et al. 1999, Haavik et al. 2000, Dubrovinsky et al. 2003, this

306   study), as well as for the $Mg_{0.5}Fe_{0.5}Fe_2O_4$ composition, implying that solid solution may be

307   complete across the $hp-FeFe_2O_4–hp-MgFe_2O_4$ binary. However, the exact phase relations for

308   the $FeFe_2O_4$ endmember are not well constrained due to the unquenchable nature of the high-

309   pressure assemblages (Schollenbruch et al. 2011).

310

311   **CHARACTERIZATION OF NEW HIGH PRESSURE PHASES**

312   Several phases with different stoichiometries have been encountered at high pressures and

313   temperatures. $(Mg,Fe)_2Fe_2O_5$ has a $CaFe_3O_5$-type structure with space group *Cmcm* like that

314   of the $Mg_2Fe_2O_5$ endmember (Boffa Ballaran et al. 2015; Evrard et al. 1980). Analogous

315   phases appear in many other simple oxide systems, either with the same (Fe_4O_5, Lavina et al.

316   2011) or a different space group [i.e. *Pbam* for $Mg_2Al_2O_5$ (Enomoto et al. 2009), $Mg_2Cr_2O_5$

317   (Ishii et al. 2014) and $Fe_2Cr_2O_5$, (Ishii et al. 2015)]. An evaluation of the structural and

318   thermodynamic properties of $(Mg,Fe)_2Fe_2O_5$ solid solutions will be the subject of a

319   companion manuscript.

320   At pressures higher than 15 GPa for the Mf50 composition and above 18 GPa for the

321   magnesioferrite end-member composition, $hp-(Mg,Fe)Fe_2O_4$ and $hp-MgFe_2O_4$ phases

322   appeared in a number of run products. Shiny black lath-shaped crystals > 50 μm were

323   recovered, but unfortunately stacking defects and retro-reaction during the quench and

324   decompression made them unsuitable for full structural refinement by single-crystal

325 diffraction. However, powder XRD patterns of both phases are inconsistent with the *Pbcm*

326 space group (No. 57) proposed for hp-$MgFe_2O_4$ by Andrault and Bolfan-Casanova (2001).

327 The structural models reported for hp-Fe_3O_4 (Fei et al. 1999; Haavik et al. 2000;

328 Dubrovinsky et al. 2003) also do not fit the XRD patterns of our samples. Instead, our results

329 are consistent with a *Pmcn* space group (No. 62), although peak overlap with coexisting

330 phases (e.g. $(Fe,Mg)_3Fe_4O_9$) adds some ambiguity to our determination. To address this

331 further, the products of experiment Z1234o were investigated by TEM. Electron diffraction

332 patterns of the [001] zone axis plane, in which it is possible to observe *hk0* reflections reveal

333 the absence of diffraction spots with h + k = 2n + 1 (e.g. 210 and $2\bar{1}0$), but with strong

334 intensities for h + k = 2n (Fig. 7a). In the $[h00]^*$ direction, diffraction spots follow the

335 extinction rule of h = 2n (Fig. 7b). These observations allow us to confirm that hp-$MgFe_2O_4$

336 [and likely hp-$(Mg_{0.5}Fe_{0.5})Fe_2O_4$] has an orthorhombic unit cell belonging to the *Pmcn* space

337 group. Unit-cell parameters and *d*-spacing of the hp-$MgFe_2O_4$ phase present in sample H4088

338 have been obtained by means of a LeBail refinement of the powder diffraction pattern using

339 the space group *Pmcn* and are compared with those reported by Andrault & Bolfan-Casanova

340 (2001) for the same phase in Table 3. Since the sample analysed by Andrault & Bolfan-

341 Casanova (2001) was synthesized at ~20 GPa and a temperature of ~2500 K, it is conceivable

342 that their hp-polymorph with a $CaMn_2O_4$ type structure could have its own stability field or

343 that it transforms to the *Pmcn* polymorph during quenching.

344 The *Pmcn* crystal structure has been also reported for hp-$FeCr_2O_4$ (Ishii et al. 2014). When

345 they compared their results from quench and in situ experiments, they concluded that their hp-

346 polymorph had the CF-type structure at pressure and temperature and that it reverted to a

347 modified CF-type structure (mCF) with *Pmcn* space group during pressure release after the

348 quench (Ishii et al. 2014). However, also the structural model of the modified CF-type

349 $FeCr_2O_4$ phase does not fit our diffraction data.

350 The addition of Fe^{2+} to the hp-$MgFe_2O_4$ endmember leads to a shortening of the *b*-parameter

351 and an extension of the *c*-parameter that compensate for each other such that the resulting

352 molar volumes do not vary appreciably (Table 4). It appears that slightly smaller volumes are

353 favored at higher temperatures.

354 A phase with $(Mg,Fe)_3Fe_4O_9$ stoichiometry is observed in both Fe^{2+}-free and Fe^{2+}-bearing

355 bulk compositions. Refinement of powder diffraction patterns reveals that it is isostructural

356 with the Fe_7O_9 phase as recently reported by Sinmyo et al. (2016). This phase has the

357 $Ca_3Tl_4O_9$-type structure (Goutenoire et al. 1995), with a monoclinic unit-cell belonging to the

358 C2/m (No. 12) space group (Table 3). In their study, Sinmyo et al. (2016) also synthesized a

359 Mg-Fe^{2+} solid solution with a composition of $(Mg_{1.06},Fe^{2+}_{1.94})Fe_4O_9$. An O_9-phase has been

360 observed in several of our diffraction patterns both in the Fe^{2+}-free system, representing the

361 Mg-endmember of Fe_7O_9 (i.e. $Mg_3Fe_4O_9$), and in Fe^{2+}-bearing samples, implying that

362 complete Mg-Fe^{2+} solid solution also is likely for this phase. The structural response to Mg-

363 Fe^{2+} substitution is mostly reflected in changes in the *a*- and *c*-parameters, although no clear

364 systematics are apparent with composition, suggesting variable cation distributions as a

365 function of synthesis conditions (Tables 3 and 4).

366

367 **IMPLICATIONS**

368 The occurrence of simple spinel-structured oxides like magnetite, chromite or spinel as

369 inclusions in diamond or in meteorites demonstrates their relevance for understanding

370 processes within the Earth and other planets. Experimental studies on such phases can be

371 directly used to place constraints on the maximum pressure and temperature at which a given

372 sample formed. The report of naturally occurring high-pressure polymorphs is much rarer,

373 with only hp-$FeCr_2O_4$ identified in the Suizhou shocked meteorite by Chen et al. (2003). In

374 this case, both the $CaFe_2O_4$-type and $CaTi_2O_4$-type structures were found. The preservation

375 of hp-phases in terrestrial samples is most likely to be compromised by phase transformations

376 occurring during exhumation. In this case, the study of textures and microstructures is

377 required in order to infer a previous high-pressure history. For example, Wirth et al. (2014)

378 describe the occurrence of a (Mg,Fe)O inclusion in a diamond from Juina Province, Brazil in

379 which magnesioferrite appears to have exsolved along dislocations and at the diamond-

380 (Mg,Fe)O interface. On textural grounds, they suggest that the magnesioferrite formed during

381 upwelling from a precursor hp-polymorph and that the diamond and (Mg,Fe)O inclusion had

382 an origin in the lower mantle. However, experiments in the $MgFe_2O_4$ system by Uenver-

383 Thiele et al. (2017) demonstrated that no direct transformation from a hp-polymorph to a

384 spinel-structured phase is possible (also see Fig. 1). On the other hand, Wirth et al. (2014)

385 report a composition close to $Mg_{0.5}Fe_{0.5}Fe_2O_4$, which opens the question of whether the

386 phase relations might be different compared to $MgFe_2O_4$. Our new results for the

387 $Mg_{0.5}Fe_{0.5}Fe_2O_4$ composition can now be directly applied to this inclusion. Although hp-

388 $Mg_{0.5}Fe_{0.5}Fe_2O_4$ is found to be stable at high pressure, there is still no common phase

389 boundary with magnesioferrite (Fig. 4). It is conceivable that metastable behavior during

390 rapid uplift from the transition zone could have permitted a direct transformation to occur. If

391 this were the case, the width of the $(Mg,Fe)_2Fe_2O_5 + Fe_2O_3$ stability field depicted in Figure

392 5 implies that hp-$Mg_{0.5}Fe_{0.5}Fe_2O_4$ must have metastably persisted over a depth range of

393 ~150 km (from about 15 to 11 GPa). However, our observation of hp-$MgFe_2O_4$ beginning to

394 react to $Mg_3Fe_4O_9 + Fe_2O_3$ within a few hours in an experiment where the temperature

395 unintentionally decreased suggests that there is little or no kinetic barrier to the breakdown of

396 the high-pressure phase (sample H4088, Fig. 2b). Thus, we concur with our previous

397 conclusion that no simple phase transition could have occurred and that the precursor to the

398 "magnesioferrite" was likely $(Mg,Fe)_2Fe_2O_5$. We note that Wirth et al. (2014) found an

399 additional phase intimately associated with their platelets of $(Mg_{0.5}Fe_{0.5})Fe_2O_4$, suggesting

400 that the precursor phase may have had a stoichiometry different from that of spinel.

401   Although the occurrence of "magnesioferrite" within (Mg,Fe)O inclusions in the study of

402   Palot et al. (2016) is similar to that described by Wirth et al. (2014), there are also textural and

403   compositional differences. Palot et al. (2016) report magnesioferrite of approximate

404   composition $Mg(Fe_{0.75},Cr_{0.17},Al_{0.08})_2O_4$ located on dislocations and as 10-20 nm euhedral

405   octahedral crystals distributed within the (Mg,Fe)O host. Considering the phase relations

406   described here, along with those for the $MgFe_2O_4$ (Uenver-Thiele et al. 2017) and for

407    $MgCr_2O_4$ (Ishii et al. 2015), we can rule out the crystallization of a spinel-structured phase at

408   upper lower mantle conditions as proposed by Palot et al. (2016). Even if hp-$MgFe_2O_4$ is

409   considered to have initially exsolved from the (Mg,Fe)O, it is unlikely that an euhedral crystal

410   form would have been preserved as it first reacted to form $Mg_2Fe_2O_5$ + Fe_2O_3, followed by a

411   second reaction to magnesioferrite during further decompression (i.e. an upwelling path

412   starting at > 20 GPa and ending at upper mantle pressures of < 9 GPa, Figs 1 and 5). The

413   octahedral crystal form is also inconsistent with the morphologies of either $Mg_2Fe_2O_5$ or hp-

414    $MgFe_2O_4$ encountered in our experiments (Figs 2 and 4). Depending on the *P-T* trajectory of

415   the upwelling, a $(Mg,Fe)_3Fe_4O_9$ phase might also be implicated in addition, or instead of

416    $Mg_2Fe_2O_5$. Based upon the now available experimental data, the most plausible model for the

417   origin of the magnesioferrite in the sample of Palot et al. (2016) would be direct precipitation

418   of the spinel-structured phase by partial oxidation of (Mg,Fe)O at pressures < ~9 GPa in the

419   upper mantle.

420   A further natural occurrence of relevance for our study was recently described by Jacob et al.

421   (2016) from the Orapa Mine, Botswana. In a framesitic diamond they found pyrrhotite

422   inclusions that have a partially developed nanocrystalline ~200 nm thick reaction corona of

423   magnetite of virtually endmember composition (Jacob, pers. comm.). In one case, they

424   observed epitaxy between the sulfide, magnetite and diamond and concluded that magnetite

425   formed at the expense of the pyrrhotite, followed by diamond nucleation on the magnetite

426   rim. This implies a direct link between the magnetite and diamond formation. Further textural

427 evaluation using Transmission Kikuchi Diffraction (TKD) revealed the presence of twinning

428 in the magnetite similar to that observed by Schollenbruch et al. (2011) in samples that had

429 reverted to magnetite due to retrograde reaction during the decompression of their

430 experiments. Jacob et al. (2016) interpreted the twinning to be evidence for a hp-Fe_3O_4

431 precursor phase on which the diamond had formed. However, the in situ study of Woodland

432 et al. (2012) demonstrated that magnetite breaks down at high pressure to the unquenchable

433 assemblage of Fe_4O_5 + Fe_2O_3 rather than hp-Fe_3O_4. Therefore, the twinning on {311} planes

434 observed by Schollenbruch et al. (2011) and also by Myhill et al. (2016) was a consequence

435 of back reaction from Fe_4O_5 + Fe_2O_3 and Fe_4O_5 + O_2, respectively . Thus, we consider the

436 observations of Jacob et al. (2016) to provide the first indirect evidence for the natural

437 occurrence of a phase with O_5-stoichiometry. Since there is no particular reason for hematite

438 to have been present in the exact 1:1 molar ratio to produce a magnetite bulk composition, it

439 is likely that Fe_4O_5 had formed on the pyrrhotite and subsequently underwent oxidation as it

440 reverted to magnetite. In the presence of a C-bearing fluid the coupled redox-reaction, 6

441 Fe_4O_5 + CO_2 = C + 8 Fe_3O_4 could also have been responsible for precipitation of diamond.

442 Myhill et al. (2016) bracketed the minimum stability of Fe_4O_5 at 8 GPa and 1200-1300 °C.

443 As magnetite remains stable up to ~10 GPa at such temperatures (Schollenbruch et al. 2011),

444 this would constrain the conditions of diamond formation to lie between 8 and 10 GPa in this

445 scenario where Fe_4O_5 can coexist with magnetite. Thus, it seems likely that "post-spinel"

446 oxide phases may play a role in redox reactions leading to diamond formation in the deep

447 upper mantle and transition zone. However, their inferred detection requires careful

448 assessment of microstructures in addition to compositional and crystallographic

449 measurements. We expect a steady increase in reports for (precursor) phases with O_5-

450 stoichiometry in inclusions in diamond as analytical techniques like TKD become routine

451 tools.

452

461 **REFERENCES CITED**

462 Akaogi, M., Hamada, Y., Suzuki, T., Kobayashi, M., and Okada, M. (1999) High pressure

463 transitions in the system $MgAl_2O_4$–$CaAl_2O_4$: a new hexagonal aluminous phase with

464 implication for the lower mantle. Physics of the Earth and Planetary Interiors, 115, 67–77.

465

466 Andrault, D., and Bolfan-Casanova, N. (2001) High-pressure phase transformations in the

467 $MgFe_2O_4$ and Fe_2O_3-$MgSiO_3$ systems. Physics and Chemistry of Minerals, 28, 211-217.

468

469 Armstrong, J.T. (1993) Matrix correction program CITZAF, Version: 3.5, California Institute

470 of Technology

471

472 Ballhaus, C. & Frost, B.R. (1994). The generation of oxidized CO_2-bearing basaltic melts

473 from reduced CH_4-bearing upper-mantle sources. Geochimica et Cosmochimica Acta, 58,

474 4931-4940.

475

476   Boffa Ballaran, T., Uenver-Thiele, L., Woodland, A.B., and Frost, D.J. (2015) Complete

477   substitution of Fe^{2+} by Mg in Fe_4O_5: The crystal structure of the $Mg_2Fe_2O_5$ end-member.

478   American Mineralogist, 100, 628-632.

479

480   Brey, G.P., Bulatov, V., and Girnis, A. (2008): Geobarometry for peridotites: experiments in

481   simple and natural systems from 6 to 10 GPa. Journal of Petrology, 49, 3–24.

482

483   Chen, M., Shu, J., Mao, H-k., Xie, X., and Hemley, R.J. (2003) Natural occurrence and

484   synthesis of two new postspinel polymorphs of chromite. Proceeding of the national academy

485   of sciences, 100, 14651-14654.

486

487   Dieckmann R. (1982). Defects and Cation Diffusion in Magnetite (IV): Nonstoichiometry and

488   Point Defect Structure of Magnetite ($Fe_{3-\delta}O_4$). Bericht der Bunsenges. Journal of Physical

489   Chemistry, 86, 112-118.

490

491   Dubrovinsky, L.S., Dubrovinskaia, N.A., McCammon, C., Rozenberg, G. Kh., Ahuja, R.,

492   Osorio-Guillen, J.M., Dimitriev, V., Weber, H.-P., Le Bihan, T., and Johansson, B. (2003)

493   The structure of the metallic high-pressure Fe_3O_4 polymorph: experimental and theoretical

494   study. Journal of Physics: Condensed Matter, 15, 7697-7706.

495

496   Enomoto, A., Kojitan,i H., Akaogi, M., Miura, H., and Yusa, H. (2009) High-pressure

497   transitions in $MgAl_2O_4$ and a new high-pressure phase of $Mg_2Al_2O_5$. Journal of Solid State

498   Chemistry, 182, 389–395.

499

500   Fei, Y., Frost, D.J., Mao, H.-K., Prewitt, C.T., and Häusermann, D. (1999) In situ structure

501   determination of the high-pressure phase of Fe_3O_4. American Mineralogist, 84, 203-206.

502

503   Frost, D.J. (2003) The structure and sharpness of $(Mg,Fe)_2SiO_4$ phase transformations in the

504   transition zone. Earth and Planetary Science Letters, 216, 313-328.

505

506   Frost, D.J., and McCammon, C.A. (2008) The redox state of Earth's mantle. Annual Reviews

507   of Earth and Planetary Sciences, 36, 389–420.

508

509   Goutenoire, F., Caignaert, V., Hervieu, M., and Raveau, B. (1995) The Calcium Thallate

510    $Ca_3Tl_4O_9$, an intergrowth of the $CaTl_2O_4$ and $Ca_2Tl_2O_5$ structures, member n = 1.5 of the

511   series $Ca_nTl_2O_{n+3}$. Journal of Solid State Chemistry, 119, 134-141.

512

513   Haavik, C., Stølen, S., Fjellvag, H., Hanfland, M., and Häusermann, D. (2000) Equation of

514   state and ist high-pressure modification: Thermodynamics of the Fe-O system at high

515   pressure. American Mineralogist, 85, 514-523.

516

517   Harte, B., Harris, J.W., Hutchison, M.T., Watt, G.R., and Wilding, M.C. (1999) Lower mantle

518   mineral associations in diamonds from São Luiz, Brazil. In: Mantle Petrology: Field

519   Observations and High Pressure Experimentation. The Geochemical Society, Special

520   Publication, 6, 125-153.

521

522   Inoue, T., Irfune, T., Higo, Y., Sanehira, T., Sueda, Y., Yamada, A., Shinmei, T., Yamazaki,

523   D., Ando, J., Funakoshi, K., and Utsumi, W. (2006) The phase boundary between wadsleyite

524   and ringwoodite in Mg_2SiO_4 determined by in situ X-ray diffraction. Physics and Chemistry

525   of Minerals, 33, 106-114.

526

527   Ishii, T., Kojitani, H., Tsukamoto, S., Fujino, K., Mori, D., Inaguma, Y., Tsujino, N.,

528   Yoshino, T., Yamazaki, D., Higo, Y., Funakoshi, K., and Akaogi, M. (2014) High-pressure

529   phase transitions in $FeCr_2O_4$ and structure analysis of new post-spinel $FeCr_2O_4$ and

530    $Fe_2Cr_2O_5$ phases with meteoritical and petrological implications. American Mineralogist, 99,

531   1788-1797.

532

533   Ishii, T., Kojitani, H., Fujino, K., Yusa, H., Mori, D., Inaguma, Y., Matsushita, Y., Yamaura,

534   K., and Akaogi, M. (2015) High-pressure high-temperature transitions in $MgCr_2O_4$ and

535   crystal structures of new $Mg_2Cr_2O_5$ and post-spinel $MgCr_2O_4$ phases with implications for

536   ultrahigh-pressure chromitites in ophiolites. American Mineralogist, 100, 59-65.

537

538   Jacob, D.E., Piazolo, S., Schreiber, A., and Trimby, P. (2016) Redox-freezing and nucleation

539   of diamond via magnetite formation in the Earth's mantle. Nature communications, 7, 11891.

540

541   Kaminsky, F.V., Wirth, R. (2011) Iron carbide inclusions in lower-mantle diamond from

542   Juina Brazil. Canadian Mineralogist, 49, 555-572.

543

544   Keppler, H., and Frost, D.J. (2005) Introduction to minerals under extreme conditions. In:

545   Miletich R. (Edt). Mineral Behaviour at Extreme Conditions. EMU Notes in Mineralogy, 7, 1-

546   30.

547

548   Kojitani, H., Enomoto, A., Tsukamoto, S., Akaogi, M., Miura, H., and Yusa, H. (2010) High

549   pressure high-temperature phase relations in $MgAl_2O_4$. Journal of Physics, Conference

550   Series, 215, 012098.

551

552   Larson, A.C., and Von Dreele, R.B. (1994) GSAS General Structure Analysis System. Los

553   Alamo National Laboratory, New Mexico, USA.

554

555   Lavina, B., Dera, P., Kim, E., Meng, Y., Downs, R.T., Weck, P.F., Sutton, S.R., and Zhao, Y.

556   (2011) Discovery of the recoverable high-pressure iron oxide Fe_4O_5. Proceedings of the

557   National Academy of Science, 108, 17281-17285.

558

559   Lavina, B., and Meng, Y. (2015) Unraveling the complexity of iron oxides at high pressure

560   and temperature: Synthesis of Fe_5O_6. Science Advances 1, no.5, e1400260.

561

562   McCammon, C., Peyronneau, J., and Poirier, J.-P. (1998) Low ferric iron content of

563   (Mg,Fe)O at high pressures and temperatures. Geophysical Research Letters, 25, 1589-1592.

564

565   Myhill, B., Ojwang, D.O., Ziberna, L., Frost, D., Boffa Ballaran, T., and Miyamjima, N.

566   (2016). On the P-T-fO$_2$ stability of Fe_4O_5 and Fe_5O_6-rich phases: a thermodynamic and

567   experimental study. Contributions to Mineralogy and Petrology, 171, 1-11.

568

569   Palot, M., Jacobsen, S.D., Townsend, J.P., Nestola, F., Marquardt, K., Miyajima, N., Harris,

570   J.W., Stachel, T., McCammon, C.A., and Pearson, D.G. (2016) Evidence for H_2O-bearing

571   fluids in the lower mantle from diamond inclusion. Lithos, in press.

572

573   Schollenbruch, K., Woodland, A.B., and Frost, D.J. (2010) The stability of hercynite at high

574   pressures and temperatures. Physics and Chemistry of Minerals, 37, 137–143.

575

576   Schollenbruch, K., Woodland, A.B., Frost, D.J., Wang, Y., Sanehira, T., and Langenhorst, F.

577   (2011) In situ determination of the spinel–post-spinel transition in Fe_3O_4 at high pressure and

578   temperature by synchrotron X-ray diffraction. American Mineralogist, 96, 820-827.

579

580   Sinmyo, R., Bykova, E., Ovsyannikov, S.V., McCammon, C., Kupenko, I., Ismailova, L., and

581   Dubrovinsky, L. (2016) Discovery of Fe_7O_9: a new iron oxide with a complex monoclinic

582   structure. Nature scientific reports, 6, 32852.

583

584   Stachel, T., Harris, J.W., and Brey, G.P. (1998) Rare and unusual mineral inclusions in

585   diamonds from Mwadui, Tanzania. Contributions to Mineralogy and Petrology, 132, 34-47.

586

587   Tobi, B.H. (2001) EXPGUI, a graphical user interface for GSAS. Journal of Applied

588   Crystallography, 34, 210-213.

589

590   Uenver-Thiele, L., Woodland, A.B., Boffa Ballaran, T., Miyajima, N. and Frost, D.J. (2017)

591   Phase relations of $MgFe_2O_4$ at conditions of the deep upper mantle and transition zone.

592   American Mineralogist, 102, 632-642.

593

594   Wirth, R., Dobrzhinetskay, L., Harte, B., Schreiber, A., and Green, H.W. (2014) High-Fe

595   (Mg,Fe)O inclusion in diamond apparently from the lowermost mantle. Earth and Planetary

596   Science Letters, 404, 365–375.

597

598   Wood, B.J., Bryndzia, L.T., and Johnson, K.E. (1990). Mantle oxidation state and its

599   relationship to tectonic environment and fluid speciation. Science, 248, 337-45.

600

601   Woodland, A.B., Kornprobst, J., and Tabit, A. (2006). Ferric iron in orogenic lherzolite

602   massifs and controls of oxygen fugacity in the upper mantle. Lithos, 89, 222-241.

603

604   Woodland, A.B., Frost, D.J., Trots, D.M., Klimm, K., and Mezouar, M. (2012) In situ

605   observation of the breakdown of magnetite (Fe_3O_4) to Fe_4O_5 and hematite at high pressures

606   and temperatures. American Mineralogist, 97, 1808-1811.

607

608   Woodland, A.B., Uenver-Thiele, L., and Boffa Ballaran, T. (2015) Synthesis of Fe_5O_6 and

609   the High-Pressure Stability of Fe^{2+}-Fe^{3+}-oxides related to Fe_4O_5. Goldschmidt Abstracts

610   2015, 3446.

611

612   **FIGURE CAPTIONS**

613

614   Figure 1. Phase relations for $MgFe_2O_4$ at 8-23 GPa and 900-1600 °C. The two experiments at

615   18 GPa and the phase boundaries at $\leq$ 18 GPa are from Uenver-Thiele et al. (2017). At 20

616   GPa and 1300-1500 °C $Mg_2Fe_2O_5$ + Fe_2O_3 converts to a hp-$MgFe_2O_4$ phase. This hp-

617   polymorph is stable over a narrow range in pressure, but widens to higher temperature. The

618   assemblage $Mg_3Fe_4O_9$ + Fe_2O_3 becomes stable between 20-23 GPa and 1300-1500 °C. The

619   phase boundaries of Levy et al. (2004) are shown for comparison.

620

621   Figure 2. Backscatter images of experimental run products performed at high pressure. a) very

622   fine grained hematite and periclase in sample Z1462u. b) large crystals of hp-$MgFe_2O_4$ with

623   interstitial phases $Mg_3Fe_4O_9$ and $Fe_2O_3.$ Lamellae and reaction rims point to an ongoing

624   reaction (see text). c) Large grain of hp-$MgFe_2O_4$ exhibiting well developed cleavage. d) hp-

625    $MgFe_2O_4$ with extensive fractures from experiment H4088. e) the most abundant phases in

626 experiment H4088 are $Mg_3Fe_4O_9$ and hematite. Compared to the hp-$MgFe_2O_4$, $Mg_3Fe_4O_9$ is

627 not strongly fractured. hem: hematite; per: periclase; hp-O_4: hp-$MgFe_2O_4$.

628

629 Figure 3. XRD pattern of sample H4088 revealing the presence of hp-$MgFe_2O_4$ (hp-O_4),

630 $Mg_3Fe_4O_9$ (O_9) and Fe_2O_3 (hem). Crosses and green solid line shows the observed and

631 calculated X-ray diffraction profiles, respectively. Tick marks beneath the diffraction pattern

632 indicate the peak positions for the different phases (from top to bottom Si standard, hp-O_4,

633 O_9, hem). At higher 2θ values diffraction peaks of hp-O_4 and O_9 phase often overlap, as

634 indicated.

635

636 Figure 4. Backscattered electron images of run products from experiments with a 50 mol%

637 $MgFe_2O_4$ - 50 mol% $FeFe_2O_4$ bulk composition are illustrated for comparison of the

638 different crystal size and shape. a) A large crystal of $Mg_{0.5}Fe_{0.5}Fe_2O_4$ spinel produced at low

639 pressure. b) Needles of the O_5 phase and fine-grained, interstitial hematite from experiment

640 M638. c) Mineral grains of $(Fe,Mg)_2Fe_2O_5$ and hematite are much more rounded. d) Lath-

641 shaped crystals of hp-$Mg_{0.5}Fe_{0.5}Fe_2O_4$. e) Large crystals of $(Mg,Fe)_3Fe_4O_9$ and hematite

642 demonstrate that the assemblage of $(Fe,Mg)_2Fe_2O_5$ + hematite is no longer stable at higher

643 temperatures. f) Aggregate of hp-$Mg_{0.5}Fe_{0.5}Fe_2O_4$. Note that crystals in low-temperature

644 experiments (e.g. samples M638 and Z1585o) are much more lath-shaped compared to those

645 found in the high-temperature experiments (e.g. samples M648 and Z1531u).

646

647 Figure 5. Phase relations of $Mg_{0.5}Fe_{0.5}Fe_2O_4$ at high pressure and temperature (in black).

648 Phase relations for the Fe_3O_4 (Woodland et al. 2012; Schollenbruch et al. 2011) and

649   MgFe$_2$O$_4$ (Uenver-Thiele et al. 2017) endmember systems are provided for comparison (in

650   grey).

651

652   Figure 6. Ternary diagram for the MgO-FeO-Fe$_2$O$_3$ system illustrating a) the phase relations

653   of run products of experiments conducted between 11-14 GPa. Run products in experiment

654   M648 include a Fe$_4$O$_5$-Mg$_2$Fe$_2$O$_5$ solid solution + hematite, along with traces of a Fe$_7$O$_9$-

655   Mg$_3$Fe$_4$O$_9$ solid solution. *Black star* indicate the Mg$_{0.5}$Fe$_{0.5}$Fe$_2$O$_4$ starting composition.

656   Dashed lines are tie-lines connecting the run products in different experiments; red lines and

657   "x" are for experiment M648 (see text). *Black dots* represent the chemical composition of

658   Fe$_4$O$_5$-Mg$_2$Fe$_2$O$_5$ solid solutions, coexisting with hematite. *Arrows* depict the path of relative

659   reduction. b) Phase relations of run products of experiments performed at > 14 GPa. Starting

660   composition for all three experiments was Mg$_{0.5}$Fe$_{0.5}$Fe$_2$O$_4$ spinel.

661

662   Figure 7. Selected area electron diffraction patterns for a crystal from sample Z1234o. a) view

663   down the [001] zone axis pattern revealing the systematic absence of diffraction spots

664   corresponding to (210) and ($2\bar{1}0$), indicating an extinction rule of (hk0): h + k = 2n.

665   Organized diffuse intensity is visible between Bragg spots.

666   b) further absences of (100) and ($\bar{1}00$) reflections as observed along the systematic [h00]*

667   direction, indicating (h00): h = 2n.

668

669

670

671

672

673

674

675

676 **TABLES**

Table 1. Experimental conditions and run products for the MgO-FeO-Fe_2O_3 system using the starting materials and stoichiometries as indicated

experimental run	pressure [GPa]	temperature [°C]	run duration [h]	run products
MgFe₂O₄ composition				
H4084[1]	18	1200	4.5	per + hem
H3889[1]	18	1300	5.5	O_5 + hem + (mgs)
Z1462u	20	1200	3	per + hem
Z1464o	20	1300[2]	0.3	hp-O_4 + O_9 + hem
Z1234o	20	1400	3	hp-O_4 + (O_5) + (hem)
H4349	20	1500	2.5	hp-O_4 + (O_5) + (hem)
H4088	23	1500	3	hp-O_4 + O_9 + hem
Mg₀.₄₉₍₂₎Fe₀.₅₁₍₂₎Fe₂O₄ composition[3]				
M650	9	1000	7	O_4
M654	10	1200	4	O_4
M649	10	1400	4.5	O_4
M638	11	1000	4	O_5 + hem
M645	11	1200	3.5	O_5 + hem
M646	12	1400	3.75	O_5 + hem
M671	12	1600	1	O_5 + hem
M648	13	1500	2	O_5 + hem + (O_9)
Z1586o	14	1100	3.5	O_5 + hem
Z1584o	15	1600	3	O_9 + hem
Z1532o	16	1400	3.5	hp-O_4
M657	18	1000	4	hp-O_4
M656	18	1500	1	hp-O_4 + [O_9]
Z1585o	20	1100	3.5	hp-O_4 + [O_9]
Z1587u	20	1200	3.5	hp-O_4 + [O_9]
Z1531u	20	1350	4	hp-O_4 + [O_9]

[1] Experiments reported in Uenver-Thiele et al. (2017). [2] Heater failed after 20 min. [3] Experiments performed with no PtO_2. O_4: $(Mg,Fe)Fe_2O_4$ with spinel structure; hp-O_4: $(Mg,Fe)Fe_2O_4$ with other structure; O_5: $(Mg,Fe)_2Fe_2O_5$; O_9: $(Mg,Fe)_3Fe_4O_9$; hem: hematite; per: periclase; phases in parenthesis: only in traces; phases in brackets: phases produced through reduction during the experimental run

Table 2a. Representative EPMA analyses (in wt%) of run products conducted with a $MgFe_2O_4$ starting material.

sample	H4088	H4088	H4349	H4349	H4349	Z1234o	Z1462u	Z1462u	Z1464o	Z1464o	Z1464o
MgO	21.24	27.57	33.72	2.27	21.30	21.12	0.78	98.74	2.95	22.00	27.12
FeO	72.76	67.34	61.49	87.48	72.81	72.69	88.88	3.38	86.52	72.42	68.42
PtO$_2$	0.08	b.d.l.	0.07	b.d.l.	b.d.l.	b.d.l.	0.12	0.02	b.d.l.	b.d.l.	b.d.l.
totals	94.08	94.91	95.28	89.75	94.11	93.81	89.78	102.14	89.47	94.42	95.54
nMg	1.00	2.94(1)	1.96(2)	0.089(1)	1.00	1.00	0.030(1)	0.980(2)	0.116(1)	1.00	2.93(5)
nFe^{2+}	0	0.06(1)	0.04(2)	-	0	0	-	0.020(2)	-	0	0.07(5)
comment	hp-$MgFe_2O_4$	$Mg_3Fe_4O_9$	$Mg_2Fe_2O_5$	hem	hp-$MgFe_2O_4$	hp-$MgFe_2O_4$	hem	per	hem	hp-$MgFe_2O_4$	$Mg_3Fe_4O_9$

Note: nMg and nFe^{2+}= number of Mg and Fe^{2+} cations per formula unit for the respective stoichiometry indicated for each column. These values are averages of multiple analyses along with 1σ errors. b.d.l= below detection limit; hem= hematite; per= periclase

Table 2b. Representative EPMA analyses (in wt%) of run products conducted with a starting mixture of $Mg_{0.5}Fe_{0.5}Fe_2O_4$.

sample	M638	M638	M645	M646	M646	M648	M648	M648	M649
MgO	13.63	0.57	12.27	14.18	0.78	12.58	0.96	14.18	9.27
FeO	81.40	89.43	83.39	80.35	88.27	84.71	89.49	83.09	85.53
PtO$_2$	b.d.l.	b.d.l.	b.d.l.	b.d.l.	b.d.l.	b.d.l.	b.d.l.	b.d.l.	b.d.l.
totals	95.03	90.002	95.66	94.53	89.05	97.29	90.45	97.27	94.80
nMg	0.914(8)	0.023(1)	0.84(1)	0.961(8)	0.034(1)	1.464(8)	0.037(1)	0.932(3)	0.484(5)
nFe^{2+}	1.086(8)	-	1.16(1)	1.039(8)	-	1.536(8)	-	1.068(3)	0.516(5)
comment	$(Mg,Fe)_2Fe_2O_5$	hem	$(Mg,Fe)_2Fe_2O_5$	$(Mg,Fe)_2Fe_2O_5$	hem	$(Mg,Fe)_3Fe_4O_9$	hem	$(Mg,Fe)_2Fe_2O_5$	$(Mg,Fe)Fe_2O_4$

Note: nMg and nFe^{2+}= number of Mg and Fe^{2+} cations per formula unit for the respective stoichiometry indicated for each column. These values are averages of multiple analyses along with 1σ errors. b.d.l= below detection limit; hem= hematite.

Table 2b. (continued)

sample	M650	M654	M656	M656	M657	M671	M671	Z1531u	Z1531u
MgO	9.54	9.41	9.00	12.13	9.50	1.36	11.03	13.43	9.54
FeO	85.11	85.99	84.93	83.06	85.17	89.93	85.53	81.45	84.42
PtO_2	b.d.l.	b.d.l.	b.d.l.	b.d.l.	b.d.l.	b.d.l.	b.d.l.	b.d.l.	b.d.l.
totals	94.65	95.40	93.93	95.19	94.67	91.29	96.56	94.88	93.96
nMg	0.499(5)	0.488(8)	0.476(12)	1.45(1)	0.498(8)	0.053(1)	0.74(1)	1.60(1)	0.509(7)
nFe^{2+}	0.501(5)	0.512(8)	0.524(12)	1.55(1)	0.502(8)	-	1.26(1)	1.40(1)	0.491(7)
comment	$(Mg,Fe)Fe_2O_4$	$(Mg,Fe)Fe_2O_4$	hp-$(Mg,Fe)Fe_2O_4$	$(Mg,Fe)_3Fe_4O_9$	hp-$(Mg,Fe)Fe_2O_4$	hem	$(Mg,Fe)_2Fe_2O_5$	$(Mg,Fe)_3Fe_4O_9$	hp-$(Mg,Fe)Fe_2O_4$

Table 2b. (continued)

sample	Z1532o	Z1584o	Z1584o	Z1585o	Z1586o	Z1586o	Z1587u	Z1587u
MgO	9.50	1.05	11.58	9.05	14.01	0.55	8.38	12.22
FeO	84.49	89.79	84.34	85.77	82.67	90.89	86.15	83.71
PtO_2	b.d.l.	0.13	b.d.l.	0.04	0.02	0.02	b.d.l.	b.d.l.
totals	93.99	90.97	95.92	94.86	96.70	91.46	94.53	95.93
nMg	0.497(5)	0.041(1)	1.37(1)	0.47(2)	0.915(11)	0.022(1)	0.443(6)	1.45(2)
nFe^{2+}	0.503(5)	-	1.63(1)	0.53(2)	1.085(11)	-	0.557(6)	1.55(2)
comment	hp-$(Mg,Fe)Fe_2O_4$	hem	$(Mg,Fe)_3Fe_4O_9$	hp-$(Mg,Fe)Fe_2O_4$	$(Mg,Fe)_2Fe_2O_5$	hem	hp-$(Mg,Fe)Fe_2O_4$	$(Mg,Fe)_3Fe_4O_9$

Table 3. Observed and calculated *d*-values of the hp-phases compared with literature data. Only *d*-values for reflections with I/Imax >1% are listed.

Phase	hp-O$_4$	hp-O$_4$	hp-O$_4$	Fe$_7$O$_9$	MgFe$_6$O$_9$	Mg$_3$Fe$_4$O$_9$
Reference	Andrault&Bolfa-Casanova (2001)	Ishii et al. (2014)	This study sample H4088	Sinmyo et al. (2016)	Sinmyo et al. (2016)	This study sample H4088
run condition	37.3 GPa, RT[1]		RT, 1 atm	RT, 1 atm	RT, 1 atm	RT, 1 atm
space group	*Pbcm*	*Pnma*	*Pmcn*	*C2/m*	*C2/m*	*C2/m*
lattice parameter						
a [Å]	2.7392(5)	9.0633(3)	2.9788(5)	9.696(2)	9.6901(12)	9.718 (3)
b [Å]	9.200(2)	2.9579(1)	9.7330(8)	2.8947(6)	2.8943(5)	2.880(1)
c [Å]	9.285(2)	10.6391(3)	10.1356(10)	11.428(3)	11.4397(15)	11.4472(12)
β [°]				101.69(2)	102.045(14)	102.11 (2)
V_{mol} [cm^3/mol]	35.23(5)	42.941(2)	44.24 (1)	94.58(4)	94.47(2)	94.31(3)
	dcalc [Å]	*dcalc* [Å]	*dobs* [Å]	*dcalc* [Å]	*dcalc* [Å]	*dobs* [Å]
	4.643	4.532	7.021	5.595	5.594	5.597
	4.122	4.169	5.068	4.083	3.293	3.351
	3.268	3.450	4.867	3.305	2.768	3.283
	2.625	3.303	4.495	2.769	2.726	2.765
	2.568	2.906	4.387	2.726	2.672	2.708
	2.526	2.850	3.510	2.681	2.664	2.680
	2.354	2.793	3.192	2.657	2.650	2.669
	2.321	2.719	3.090	2.652	2.543	2.574
	2.300	2.660	2.848	2.542	2.423	2.471
	2.285	2.627	2.775	2.425	2.422	2.454
	2.281	2.552	2.742	2.424	2.291	2.239
	2.072	2.486	2.732	2.289	2.238	2.211
	2.061	2.477	2.568	2.238		1.999
	2.043	2.412	2.534	2.221		1.702
	2.002	2.294	2.483	2.204		1.599
	1.995	2.272	2.464	2.153		1.598
	1.873	2.245	2.452	2.136		
	1.870	2.216	2.433	2.093		
		2.203	2.340	2.047		
		2.085	2.271	1.974		
		2.072	2.248	1.912		
		1.996	2.145	1.910		
		1.964	2.031	1.883		
		1.932	2.014	1.870		
		1.926	1.997	1.822		
		1.816	1.974	1.793		
		1.813	1.871	1.692		
		1.799	1.840	1.663		
		1.787	1.766	1.600		
		1.740	1.755	1.599		
		1.704	1.689	1.596		
		1.697	1.687	1.591		
		1.651	1.664			
		1.614	1.659			
		1.604	1.652			

[1]RT: room temperature

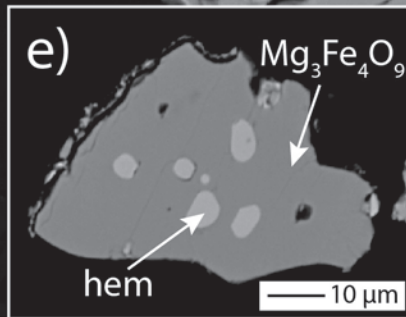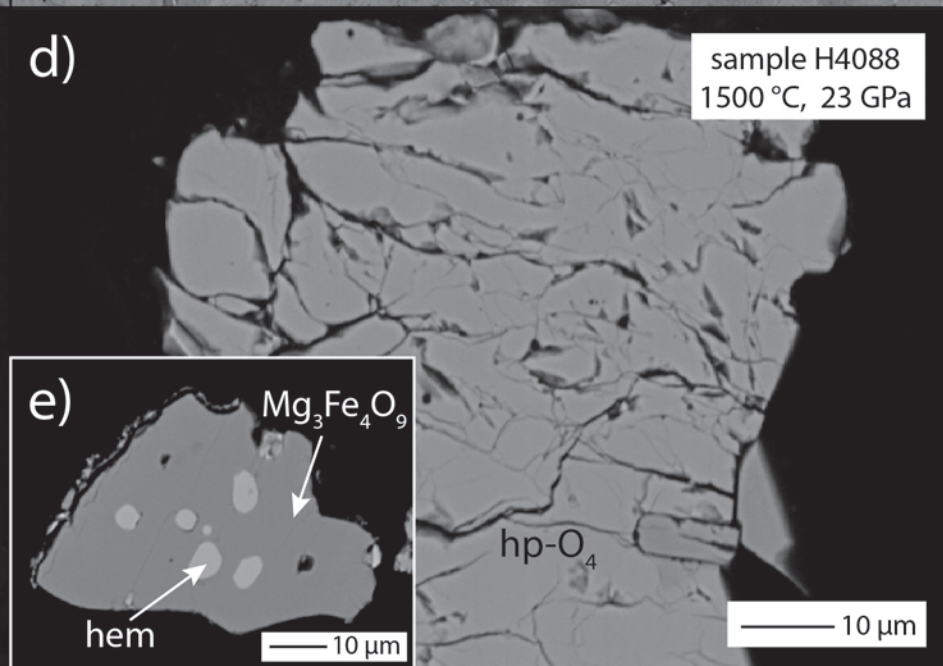Table 4. Unit cell parameters and chemical composition of the hp-$(Mg,Fe)Fe_2O_4$ and $(Mg,Fe)_3Fe_4O_9$

experimental run	hp-$(Mg,Fe)Fe_2O_4$						$(Mg,Fe)_3Fe_4O_9$						
	nMg	nFe^{2+}	a [Å]	b [Å]	c [Å]	V_{mol} [cm^3/mol]	nMg	nFe^{2+}	a [Å]	b [Å]	c [Å]	β [°]	V_{mol} [cm^3/mol]
Z1587u	0.443(6)	0.557(6)	2.9761(1)	9.6683(7)	10.2159(5)	44.254(3)	1.45(2)	1.55(2)	9.699(1)	2.8909(2)	11.4502(9)	102.145(8)	94.506(9)
Z1585o	0.473(19)	0.527(19)	2.9766(1)	9.6843(5)	10.2008(5)	44.269(3)	-	-	9.742(1)	2.872(1)	11.446(2)	102.00(1)	94.31(2)
M656	0.476(12)	0.524(12)	2.9790(6)	9.664(2)	10.211(2)	44.119(11)							
Z1532o	0.497(5)	0.503(5)	2.9793(9)	9.656(3)	10.206(3)	44.20(2)							
M657	0.498(8)	0.502(8)	2.9789(2)	9.6848(6)	10.1871(5)	44.248(3)							
Z1531u[1]	0.509(7)	0.491(7)	-	-	-	-	1.60(1)	1.40(1)	-	-	-	-	-
Z1584o							1.37(1)	1.63(1)	9.7019(7)	2.8933(2)	11.4585(8)	102.132(8)	94.687(6)
H4088	1	0	2.9788(5)	9.7330(8)	10.1356(10)	44.24 (1)	3	0	9.718(3)	2.880(1)	11.4472(12)	102.11(2)	94.31(3)
Z1234o	1	0	2.9769(4)	9.7322(13)	10.1475(15)	44.260(8)							

[1] diffraction peaks are broad and could not be used to reliably determine lattice parameters

a) sample Z1462u 1200 °C, 20 GPa — per, hem, 10 μm

b) sample Z1464o 1300 °C, 20 GPa — $Mg_3Fe_4O_9$, hem, hp-O_4, 30 μm

c) sample Z1234o 1400 °C, 20 GPa — hp-O_4, 10 μm

d) sample H4088 1500 °C, 23 GPa — hp-O_4, 10 μm

e) $Mg_3Fe_4O_9$, hem, 10 μm
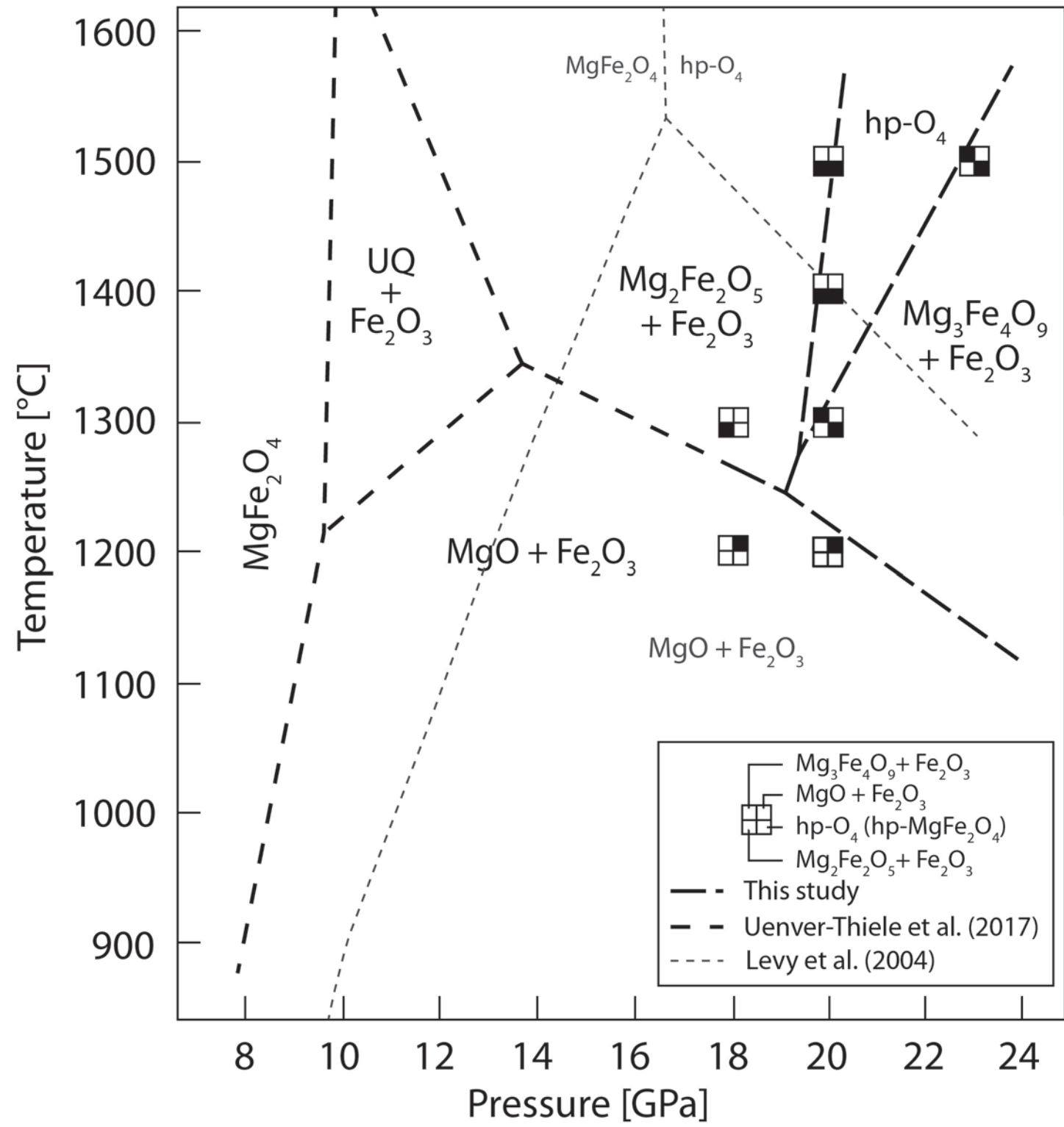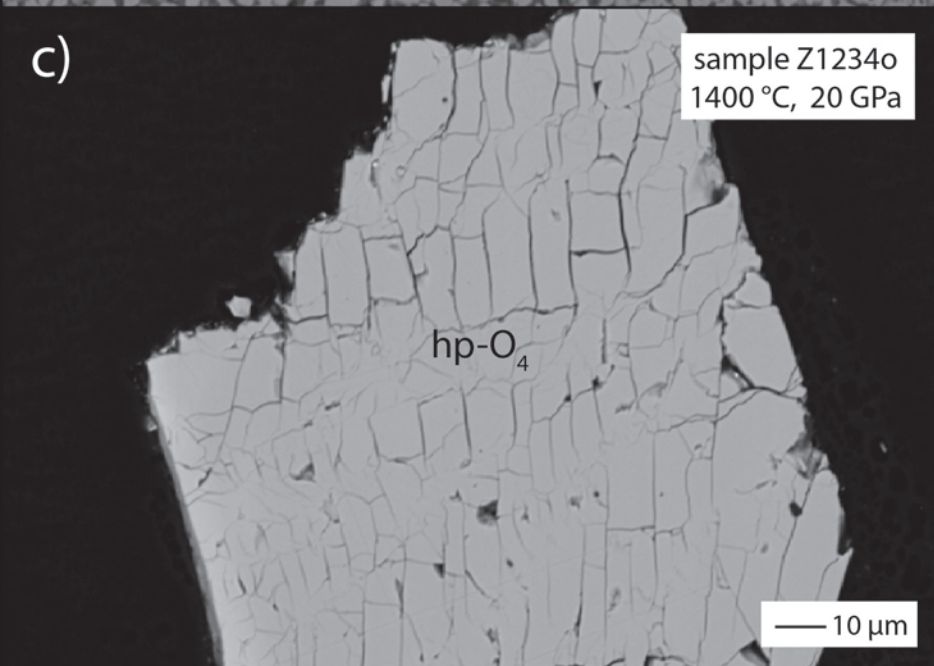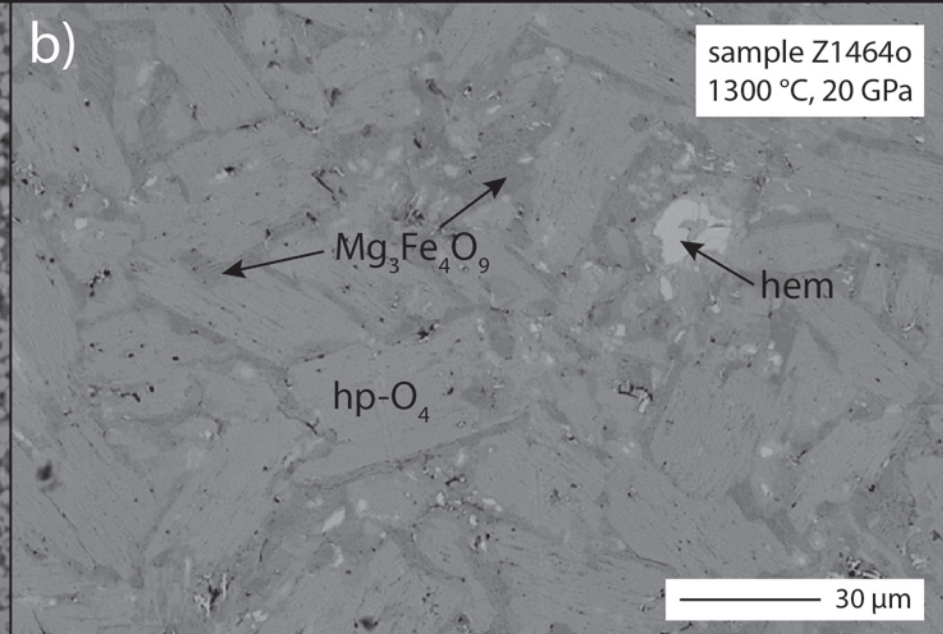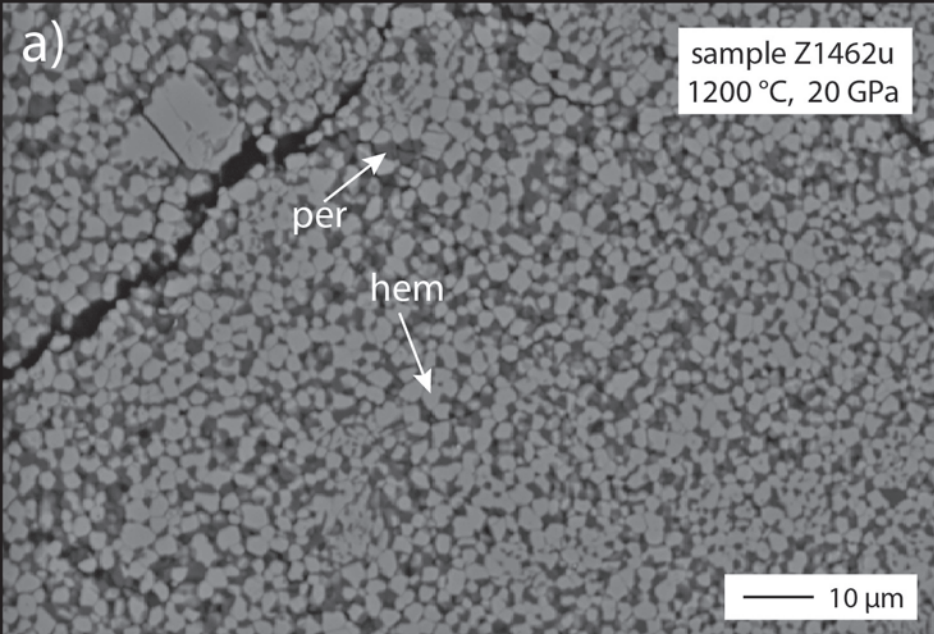
H4088   Hist 1
Lambda 1.7890 A, L-S cycle 386   Obsd. and Calc. Profiles
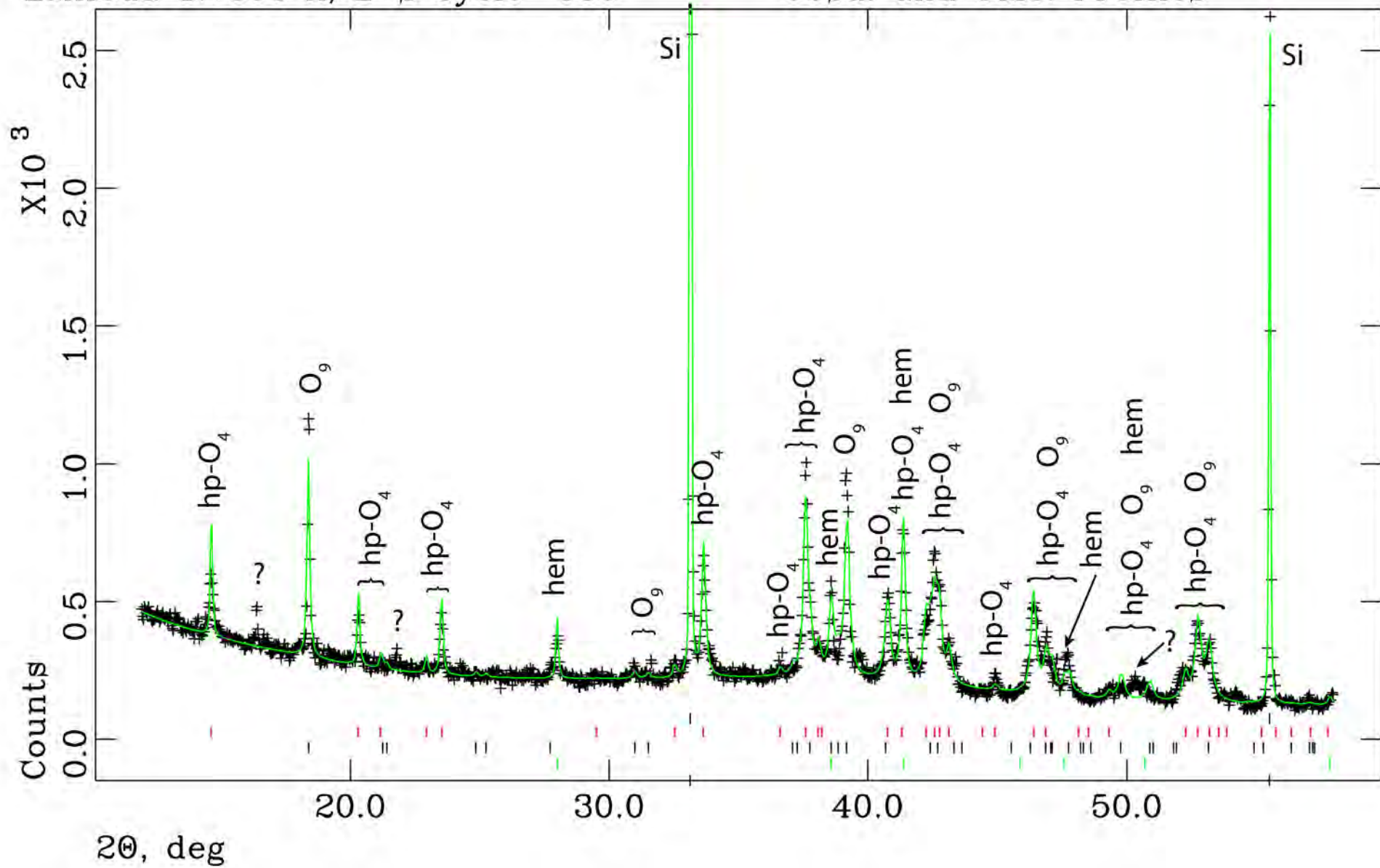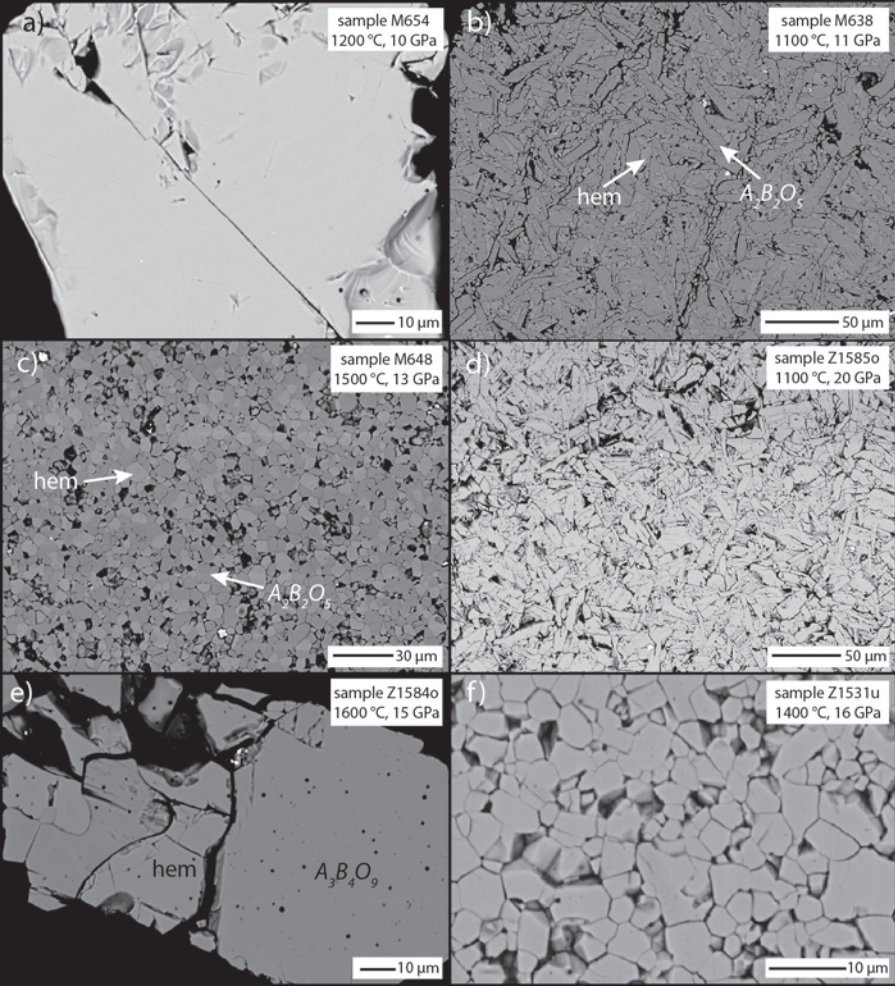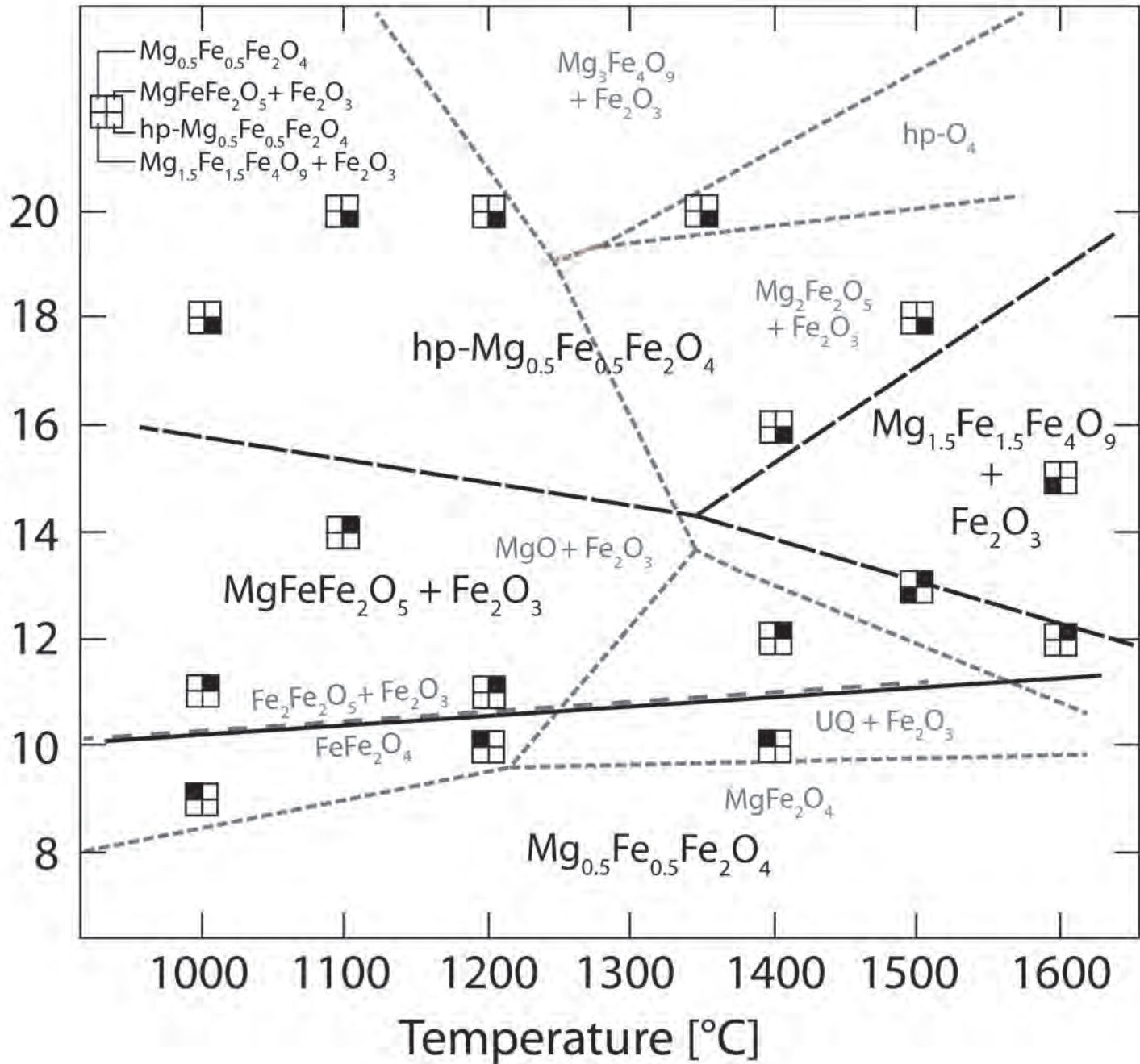
a) sample M654 — 1200 °C, 10 GPa — 10 µm

b) sample M638 — 1100 °C, 11 GPa — hem, $A_2B_2O_5$ — 50 µm

c) sample M648 — 1500 °C, 13 GPa — hem, $A_2B_2O_5$ — 30 µm

d) sample Z1585o — 1100 °C, 20 GPa — 50 µm

e) sample Z1584o — 1600 °C, 15 GPa — hem, $A_3B_4O_9$ — 10 µm

f) sample Z1531u — 1400 °C, 16 GPa — 10 µm
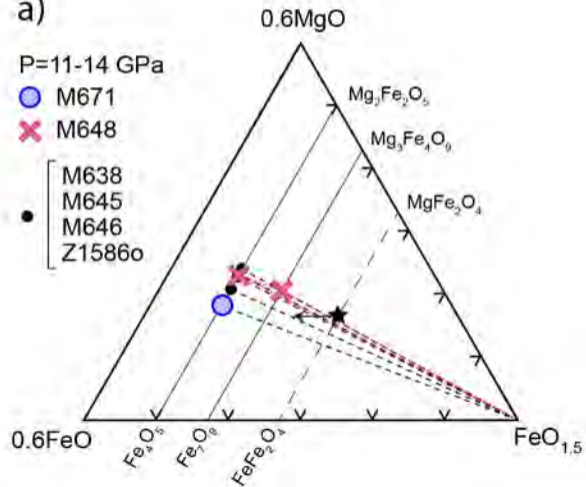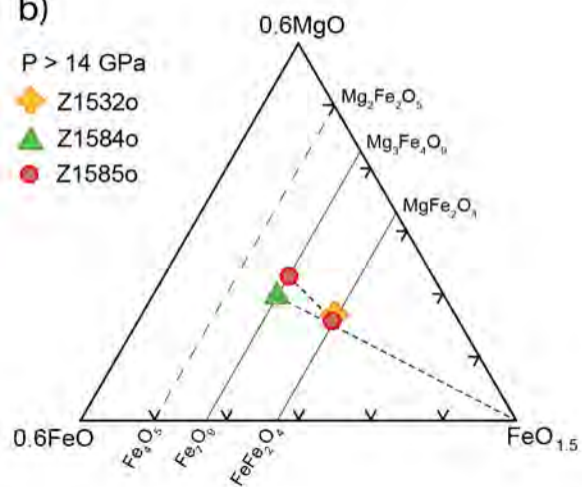
a) Absence of spots, h + k = 2n + 1
e.g. 210 or 2$\bar{1}$0

200

110

020

ZA[001]

b) 200

Absence of
100 & $\bar{1}$00

020